

# Robust time reversal focusing in the ocean

Seongil Kim,<sup>a)</sup> W. A. Kuperman, W. S. Hodgkiss, H. C. Song, G. F. Edelmann, and T. Akal<sup>b)</sup>

*Marine Physical Laboratory, Scripps Institution of Oceanography, La Jolla, California 92093-0238*

(Received 14 March 2002; revised 5 March 2003; accepted 13 April 2003)

Recent time-reversal experiments with high-frequency transmissions (3.5 kHz) show that stable focusing is severely limited by the time-dependent ocean environments. The vertical focal structure displays dynamic variations associated with focal splitting and remerging resulting in large changes in focal intensity. Numerical simulations verify that the intensity variation is linked to the focal shift induced by phase changes in acoustic waves resulting from sound speed fluctuations due to internal waves. A relationship between focal range shift, frequency shift, or channel depth changes is illustrated using waveguide-invariant theory. Based on the analysis of experimental data and numerical simulations, methods for robust time-reversal focusing are developed to extend the period of stable focusing. © 2003 Acoustical Society of America. [DOI: 10.1121/1.1582450]

PACS numbers: 43.30.Vh, 43.30.Re, 43.60.Gk [RS]

## I. INTRODUCTION

Time reversal<sup>1-4</sup> is a process of transmitting a received signal in a time-reversed order. It exploits the time-reversal invariance of the wave equation such that the retransmitted wave from a time-reversal mirror (TRM) converges back to the position of a probe source (PS) where the signal was generated. The fact that time-reversal processing (TRP) both spatially and temporally refocuses the acoustic energy in a complicated ocean environment suggests possible applications to future active sonar and underwater communication systems.

Since TRP utilizes the advantage of reciprocity in a static medium, the performance can be degraded in a non-static environment,<sup>5,6</sup> where the propagation conditions change during the time between the forward propagation of a probe signal and the backpropagation of the time-reversed signal. In recent experiments, the stability of the focal structure was investigated by repeatedly retransmitting a stored probe source pulse into the time-dependent ocean medium. While the focal structure was maintained over several hours to days with low-frequency (445 Hz) transmissions,<sup>7</sup> measurements with high-frequency (3.5 kHz) transmissions showed that the stable focus was limited to on the order of a few tens of minutes, implying that the effect of medium fluctuation is not trivial for such high-frequency transmissions.

The ability to maintain a stable focus is important in the applications of TRP. In underwater communications it is desirable to extend the period of reliable communications using a single probe pulse captured in order to increase the data rate by increasing the time intervals between the training probe pulses.<sup>8</sup> Similarly, in the acoustic barrier concept,<sup>9</sup> a disturbance between the TRM and the focus can be monitored continuously over an extended period of time without

refreshing the TRM focus. The analogy between TRP and matched-field processing (MFP) also can provide useful guidance for developing more robust MFP methods.

Our objective in this paper is to develop an efficient method for robust time-reversal focusing in a fluctuating ocean environment. To achieve this, the experimental data are analyzed to extract the main features of focal stability. The detailed response of the time-reversal focus to sound-speed fluctuations driven by internal waves is then examined using numerical simulations. A simple theory based on waveguide invariants<sup>10-13</sup> can describe the relationship between focal stability and the changes in environmental conditions. Finally, based on the analysis of experimental and numerical simulations, methods for robust time-reversal focusing are developed to extend the period of stable focusing.

In the next section, focal resolution and stability of ocean acoustic time reversal are reviewed briefly. In Sec. III, time-reversal experiments and the measured focal stability in a fluctuating ocean are described. In Sec. IV, the effect of sound-speed fluctuations on the spatial focal structure is investigated using numerical simulations. In Sec. V, a theoretical analysis based on waveguide invariant theory is examined to describe the focal shift caused by sound-speed variations. In Sec. VI, robust time-reversal methods are explored using multiple constraint methods.

## II. OVERVIEW OF OCEAN TIME-REVERSAL ACOUSTICS

Here, we briefly describe the concept of time-reversal processing, focal size, and the effect of sound-speed fluctuations on the focal structure. Additional details about the general concept of ocean TRP and the analogy with matched-field processing can be found in Refs. 4 and 14.

TRP involves two-way wave propagation between a probe source and a time-reversal mirror, as depicted in Fig. 1. The TRM refocuses wave energy back to the position where the signal was generated. The signal can be a man-made sound, natural noise, or scattered sound from rough ocean boundaries, etc. In the experiments, we used a PS to

<sup>a)</sup>Presently S. Kim is with the Agency for Defense Development, Chinhae 645-600, South Korea. Electronic mail: sikim@add.re.kr

<sup>b)</sup>This work was done while at the SACLANT Undersea Research Center, 19138 La Spezia, Italy. Current address: TUBITAK-MAN, Marmara Research Center, Earth and Marine Sciences Research Institute, P.K.21 Gebze, Kocaeli 41470, Turkey.

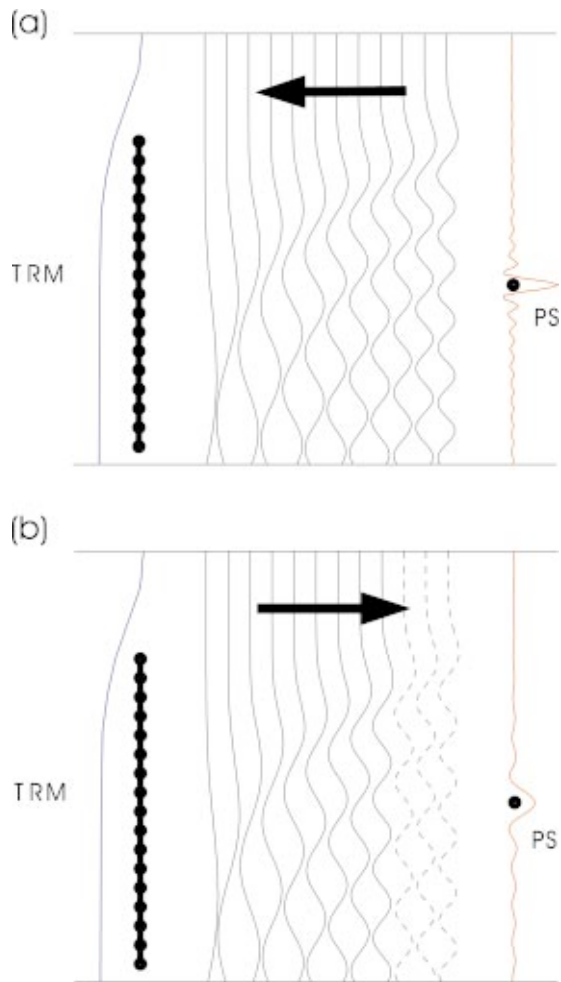


FIG. 1. Schematic of time-reversal processing: (a) a probe signal is excited and propagates to the TRM; (b) time-reversed signal propagates backward from the TRM.

generate an initial pulse. The excited acoustic field can be decomposed into modes and each mode propagates with its own group speed. In general, the lower-order modes propagate faster in shallow water and arrive earlier at the TRM. The received signal exhibits dispersion patterns in time. After amplifying the received signal, the TRM retransmits the time-reversed version of the signal (last in, first out). During the two-way propagation between the PS and TRM, some higher-order modes that have more interactions with an ocean bottom are removed by waveguide attenuation. Then, the remaining modes arrive simultaneously at the range of the PS and realize a focus at the original position.

The focal size or the resolution<sup>15</sup> of a TRM is determined by the remaining effective modes. The focal size in depth and range can be estimated roughly as

$$\Delta_z \sim \frac{D}{M}, \quad (1)$$

$$\Delta_R \sim \frac{2\pi}{k_1 - k_M}, \quad (2)$$

where  $D$  is water depth,  $M$  is the number of effective modes, and  $k_1$  and  $k_M$  are the horizontal wave numbers of the first and last effective modes, respectively. The vertical resolution

is determined by the mode functions while the horizontal resolution is determined by the difference of wave numbers that is the smallest *interference pattern* of the acoustic field. Waveguide attenuation increases the focal size by reducing the number of effective modes. The focal size is also proportional (inversely proportional) to the wavelength (frequency). The focal sizes have been shown to approach the diffraction limit of the TRM in a static ocean.<sup>15</sup>

In a nonstatic medium where sound propagates through different environments each way, sound-speed fluctuations change the mode functions as well as the horizontal wave numbers. The mode functions determine the amplitude of the acoustic field while the horizontal wave numbers are associated with the phase of the wave field. Acoustic fields are very sensitive to small changes in the phase terms, indicating that the horizontal focal structure is vulnerable to sound-speed fluctuations. Changes in horizontal wave numbers cause perturbed group speeds resulting in delays or advances of mode arrivals. The detailed focal structure response to the sound-speed fluctuation is investigated in Sections III and IV.

### III. TIME-REVERSAL EXPERIMENTS

In this section, we describe the measured time-reversal foci in a time-evolving ocean environment. The results show that the effect of ocean fluctuations on the time-reversal focus is not negligible in the high frequency (3.5 kHz) transmissions.

#### A. Experimental setup

A series of time-reversal experiments was performed in two areas near Formiche and Elba islands off the west coast of Italy depicted as shaded boxes in Fig. 2. Both areas are relatively flat environments with a water depth of about 130 m in the Formiche area and 120 m in the Elba area, respectively. A detailed oceanographic survey was accompanied by deploying thermistor chains, wave riders, current meters, etc. Sound-speed profiles (SSP) also were measured frequently by conductivity-temperature-depth (CTD) casts. The SSPs collected over the experiment period indicate variability of the upper water column, especially in the thermocline region. The downward-refracting sound speed structure resulted in a substantial interaction of the sound field with the ocean bottom. This also suggests that acoustic fluctuations are dominated by sound-speed fluctuations caused by internal waves rather than surface wave effects.

Figure 3 shows the components of a TRM experiment. The detailed hardware configurations for the low- and high-frequency TRMs can be found in Refs. 4 and 16, respectively. The TRM received an incident signal from a probe source (PS) and retransmitted the time-reversed signal to the vertical receiver array (VRA) that was collocated with the PS. In the April 1996 and May 1997 experiments, a TRM was deployed near the island of Formiche di Grosseto. The TRM spanned 77 m of the water column with 20 receiving hydrophones and 20 contiguously located slotted cylinder sources. Each element of the TRM was operated at a nominal source level of 160 dB *re* 1  $\mu$ Pa per transducer with a center frequency of 445 Hz. A PS was located in the vicinity of a 48-element VRA. The July 1999 experiment was performed

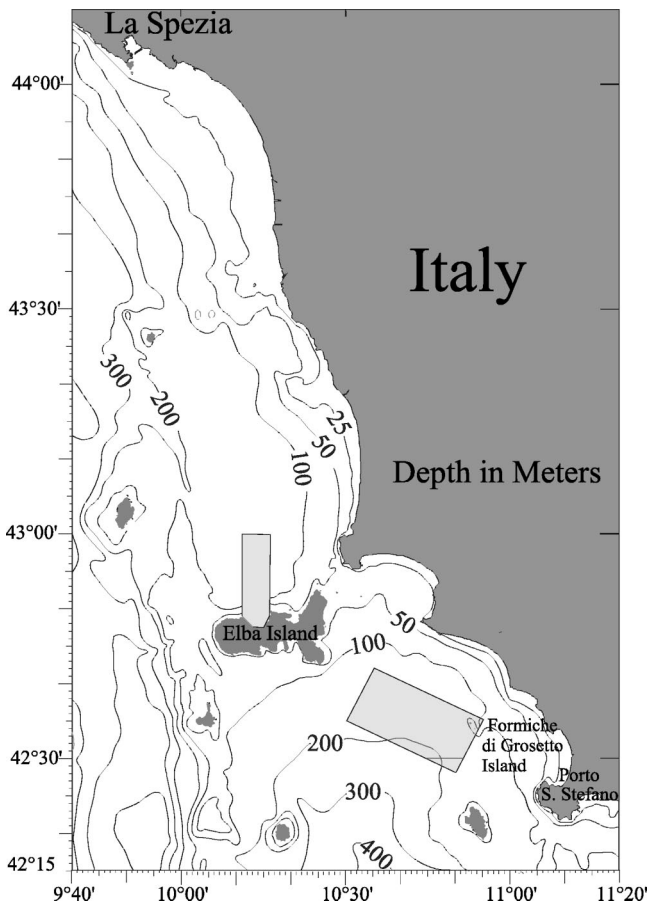


FIG. 2. Locations of the time-reversal experiments. Low-frequency (445 Hz) experiments were performed near Formiche di Grosseto and high-frequency (3.5 kHz) experiments were carried out both in the Formiche and Elba areas.

with a center frequency of 3.5 kHz in both the Formiche and Elba areas and the May/June 2000 experiment was performed in the Elba area. The experimental setup was similar to the lower-frequency experiments but the TRM had 29 transducers spanning a 78 m aperture with a nominal source level of 180 dB *re* 1  $\mu$ Pa per transducer. The VRA covered 93 m of the water column with 32 hydrophones.

### B. Time-reversal foci in a fluctuating ocean

If the ocean is static, PS pulses can be stored ahead of time to focus at specific locations. However, the temporal variability of the ocean is expected to limit such a procedure. In the May 1997 experiment, we found that probe pulses at 445 Hz still produced a significant focus at the original probe–source location up to one week later (see Hodgkiss *et al.*<sup>7</sup> for details). But our recent experiment in May/June 2000 with 3.5 kHz transmissions showed that a stable focus was severely limited by the medium fluctuations.

Figure 4 shows the time-reversed pulses received with the VRA by retransmitting the received probe pulse after a short time (16 min), 1 day, and 1 week, respectively. The range between the TRM and PS was 15.2 km and the PS depth was 81 m. The PS signal was a 50 ms pulse at a 445 Hz carrier. The vertical focal size was about 20 m. During the period, the focus moved a few meters downward, result-

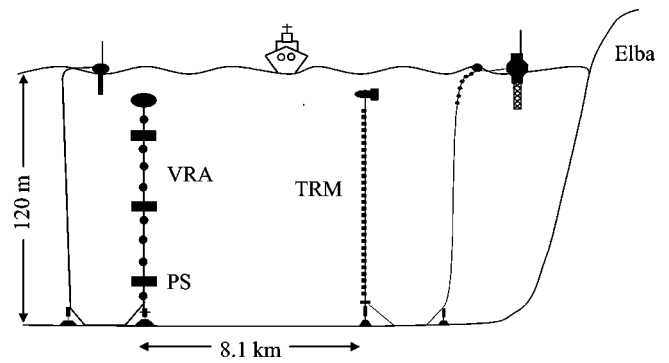


FIG. 3. Experimental setup for the high-frequency (3.5 kHz) time-reversal experiment. The time-reversal mirror (vertical source–receiver array) consisted of 29 transducers with interelement spacing 2.786 m spanning 78 m of the water column.

ing from the increased temperature in the upper part of the water column during the experiment period. Although the focus was degraded significantly after a week along with the appearance of a sidelobe in the upper water column, the TRM clearly retained a focus. This result reveals that time reversal at 445 Hz was robust in these ocean conditions.

Figure 5 shows typical examples of a probe signal received by the TRM and the corresponding focused pulse observed by the VRA after retransmitting the received signal from the TRM. The probe source was located 7.9 km away from the TRM at a depth of 43 m. The signal was a 2 ms pulse consisting of seven cycles of a 3.5 kHz carrier. The probe signal received by the TRM shows dispersion by more than 20 ms at about 10 dB down in intensity. As expected from the measured sound-speed profile, most acoustic energy is distributed in the early arrivals, i.e., in the lower-order modes, and below the thermocline, which implies substantial interactions with the bottom. The signal above 20 m depth is negligible, indicating that the interaction with the ocean surface is not important for propagation to this distance. The focused signal shows the spatial and temporal compression obtained with the time-reversal process. The vertical focal size was about 2 m and the signal length was compressed back to 2 ms at 3 dB down points.

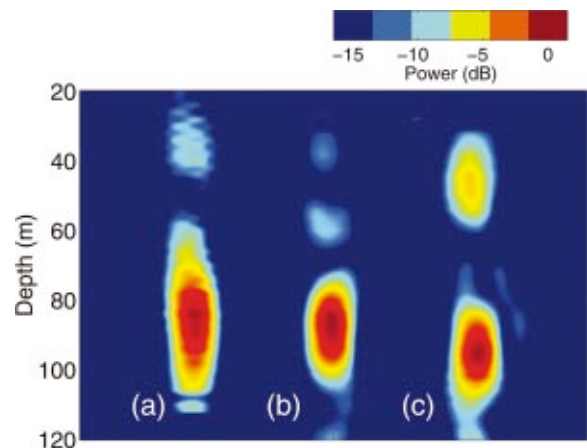


FIG. 4. Measured time-reversal foci with low-frequency (445 Hz) transmissions. A 50 ms pulse received by a TRM from a PS 15.2 km away at a depth of 81 m was retransmitted (a) 16 min, (b) 1 day, and (c) 1 week later.

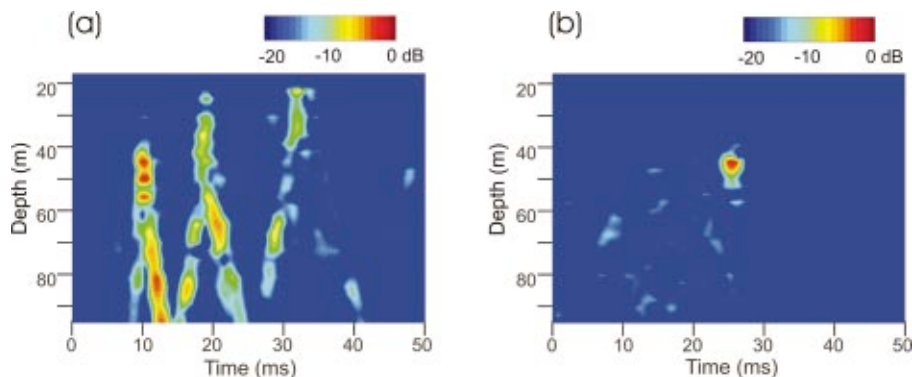


FIG. 5. Measured examples of (a) a probe signal received by the TRM and (b) a focused signal observed by the VRA. The distance between the probe source and the TRM was 7.9 km and a 2 ms pure tone pulse at 3.5 kHz was transmitted at a depth of 43 m.

We also measured the temporal variability of the focused signal with high-frequency transmissions. Figure 6(a) shows the results of high-frequency time-reversal foci obtained by retransmitting the stored PS pulse every minute over 45 min starting at 08:28 GMT on 31 May 2000. The pulse was 10 ms long and the probe source was 8.1 km away from the TRM at a depth of 68 m. The vertical focal size was less than 2 m in this case. Although the vertical focal size did not change very much, the intensity at the PS position decreases gradually to  $-7$  dB over 45 min, as shown in Fig. 6(b). In addition to the gradual decrease in intensity with time, another feature is that the focal structure shows a slight upward movement between 20 and 30 min and a corresponding sidelobe appears at a depth of around 75 m. The intensity curve at the probe source depth indicates additional degradation of the focal intensity during this short time period. This phenomenon was more prominent in the next measurement.

Another measurement (Fig. 7) obtained a few hours later (starting at 11:04 GMT on 31 May 2000) showed more unstable results of the time-reversal foci. In this case, a 2 ms pulse was generated from the PS. The PS depth was 54 m and the range was the same (8.1 km) as before. The retransmission from the TRM began 1 min after the reception of the PS pulse and lasted for 50 min. The focal structure shows more sidelobes overall. Once again, the foci moved upward between 18 and 33 min with a sidelobe below at 60 m. The foci almost were divided into two vertical structures during this time and they then were recombined into one later. The intensity level at the probe source position as shown in Fig. 7(b) decreased rapidly by  $-8$  dB during the time of the split focal structure then recovered up to  $-3$  dB at 40 min.

From the experimental results we can extract some important facts about the focal structure in a time-evolving

ocean environment. First, as expected, the high-frequency focal structure was much more sensitive to the environmental changes. Although the measurements were not sufficient to define quantitatively the relaxation time of the focal structure, it is reasonable to estimate that it was on the order of about a day with the 445 Hz transmissions and less than an hour with the 3.5 kHz transmissions in the ocean conditions of the area. Second, the focal intensity at the position of the PS did not decrease linearly with time. In a dynamic ocean environment, we observed focal splitting and recombination.

#### IV. NUMERICAL SIMULATION OF TIME-REVERSAL FOCUSING

In the previous section, we examined the variation of vertical focal structures measured with a vertical-receiver array (VRA) collocated at the position of the probe source (PS). In this section we investigate the variation of the horizontal focal structure using numerical simulations. A fundamental question is whether the focus actually disappeared or simply was somewhere else spatially during the time when we observed splitting of the focal structure. The main result of this numerical study is that a sound-speed perturbation causes a focal shift along with intensity degradation.

##### A. Procedure

Here, we describe the numerical simulation procedure. The first step is generating the time series of the sound-speed fluctuations. The major sources of acoustic fluctuations for the propagation of sound over the 10 km range and time scales of a few minutes to an hour are surface waves and internal waves. As we observed from the experimental results, surface wave effects are negligible in this downward-

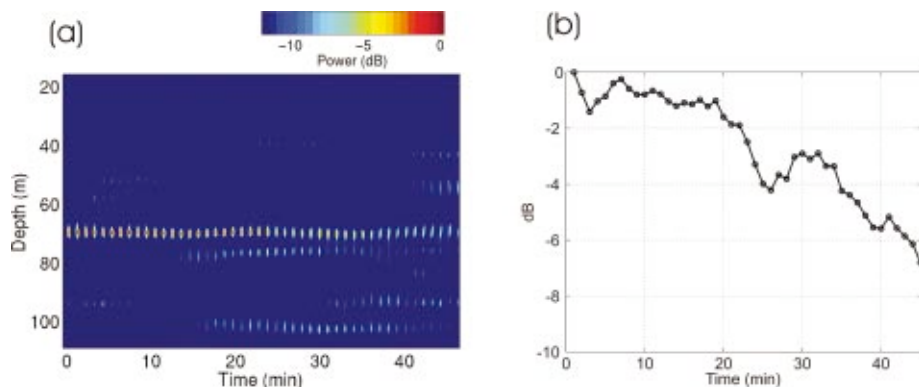


FIG. 6. Measured time-reversal stability with high-frequency (3.5 kHz) transmissions. A stored 10 ms probe pulse received by a TRM from a PS at a range of 8.1 km and a depth of 69 m was retransmitted repeatedly for 45 min; (a) the pulse signal received every minute by a vertical receiver array; (b) variation of the intensity level at the PS position.

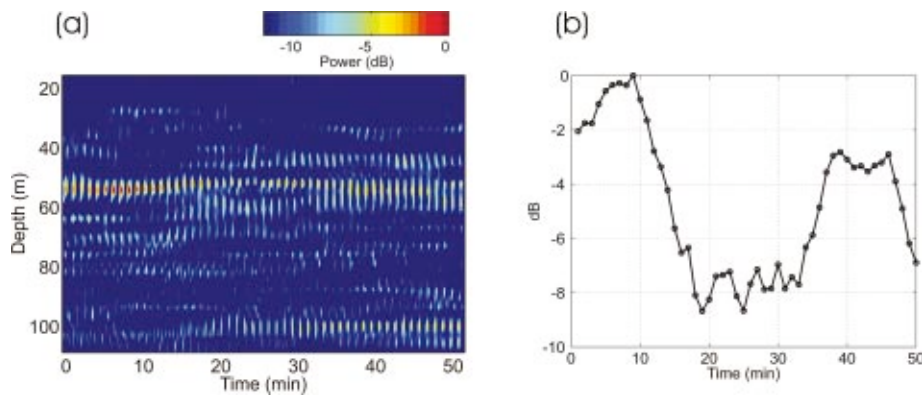


FIG. 7. The same as Fig. 6, except the probe source depth was 54 m, the pulse length was 2 ms, and the transmission lasted for 50 min.

refracting sound-speed environment. Thus, we consider only sound-speed fluctuations caused by internal waves. The sound-speed perturbation  $\delta c(r, z, t)$  is assumed to be related solely with the vertical displacement of the internal waves and is given by

$$\delta c(r, z, t) = c_p[z - \eta(r, z, t)] - c_p(z), \quad (3)$$

where  $c_p(z)$  is the potential sound speed and  $\eta(r, z, t)$  is the vertical displacement of internal waves. The method used for the calculation of  $\eta(r, z, t)$  and associated parameters are discussed in detail in the Appendix following the method developed by Henyey *et al.*<sup>17</sup> Refer to the listed articles<sup>18–20</sup> for a more thorough description of this subject. The parameters used for the generation of the internal waves were chosen to simulate the environmental condition of the May/June 2000 experiment performed near Elba Island. A representative buoyancy frequency profile in Fig. 8(b) was determined from the average value of the CTD casts obtained on 21 May 2000 near the TRM, as shown in Fig. 8(a). The maximum buoyancy frequency is about 18 cph at 25 m and exponentially decreases with depth. The power spectrum of internal waves was calculated using thermistor chain data sampled every 5

min, as shown in Fig. 8(c). An internal wave spectrum was obtained from the data set measured at 39 m. The spectrum shapes measured at the other depths were similar. The thick dashed line represents the functional form of the spectrum (see the Appendix for details) used for the internal wave simulation. The interval between the inertial frequency  $\omega_I$  and the maximum buoyancy frequency  $N_{\max}$  determines the range of the internal wave frequencies to be calculated. Figure 8(d) shows an example of simulated sound-speed profiles in range and depth. The fluctuations are mostly distributed between 20–60 m and become zero at the surface and bottom as specified by the boundary conditions. Two-dimensional sound-speed fields were calculated every minute for several hours for use as environmental input for modeling acoustic propagation.

Next, the acoustic field between the TRM and field points was calculated using a parabolic equation model.<sup>21</sup> The input sound-speed environment was range dependent, as simulated by the internal wave model. The model ocean and the array configuration were similar to the May/June 2000 experiment. The model TRM consists of 29 elements span-

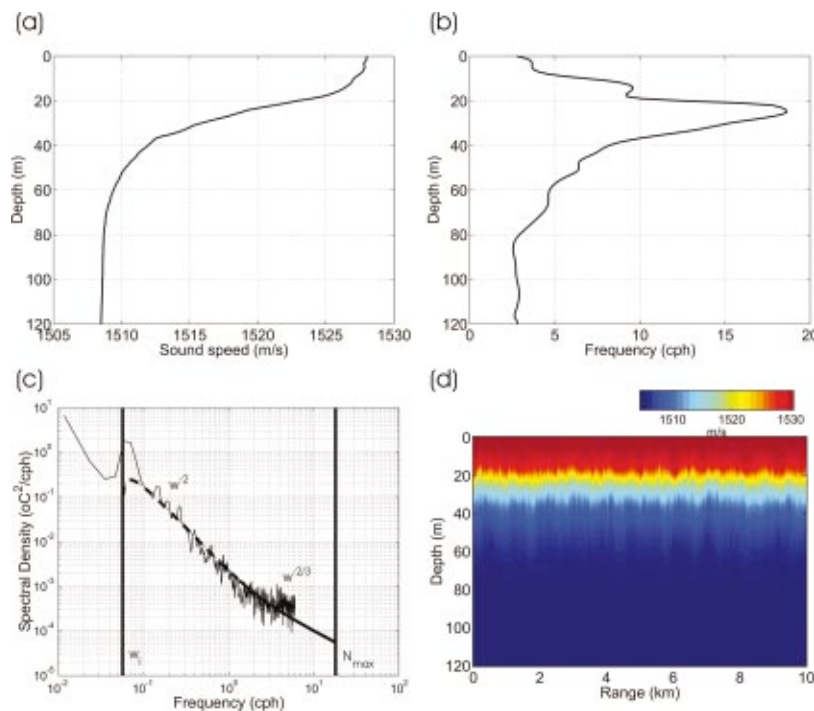


FIG. 8. Measured and simulated internal wave fields: (a) measured average sound speed profile; (b) profile of buoyancy frequency calculated from CTD data; (c) measured internal wave spectrum (solid line) and a function used for the internal wave simulation (thick dashed line); and (d) simulated sound-speed structure.

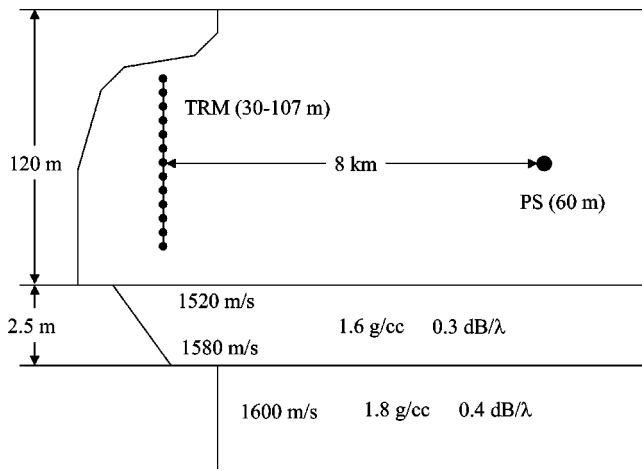


FIG. 9. Ocean waveguide parameters used for simulations of the time-reversal process. The sound speed of the water column at the bottom interface is about 1508 m/s. Thus, acoustic waves propagating above the critical angle ( $7.2^\circ$ ) are highly attenuated.

ning the 120 m deep water column from 30 to 107 m with 2.75 m interelement spacing. The PS is located at 60 m depth and is 8 km away from the TRM. The ocean bottom has a 2.5 m thick sediment layer with a sound speed at the top interface of 1520 m/s. Since the sound speed of the water column at this depth is 1508 m/s, acoustic waves propagating above the critical angle of  $7.2^\circ$  are highly attenuated. The waveguide environment used for the simulation is depicted in Fig. 9. In the PE calculation, the depth and range steps were 0.1 and 1 m, respectively, and four Padé coefficients were used. The calculations were carried out at one-minute intervals for each time frame of the internal wave-induced range-dependent sound-speed fluctuations. During the propagation time between the TRM and PS (about 5 s), we assumed the ocean environment is frozen.

The final step was to implement the time-reversal process with the calculated transfer functions between the TRM and the field points. Let the Green's function at frequency  $\omega$  and the  $j$ th element of the TRM due to a probe source located at a horizontal distance  $R$  and depth  $z_s$  be  $G(\mathbf{r}_j; \mathbf{r}_s, \omega)$ , where  $\mathbf{r}_j = (0, z_j)$  and  $\mathbf{r}_s = (R, z_s)$ . Then, the acoustic field observed at a field point  $\mathbf{r} = (r, z)$  reduces to a sum over the TRM transducer positions,

$$p(\mathbf{r}, \Delta t, \omega) = \sum_j S^*(\omega) G^*(\mathbf{r}_j; \mathbf{r}_s, t_1, \omega) G(\mathbf{r}; \mathbf{r}_j, t_2, \omega), \quad (4)$$

where  $S(\omega)$  is the source spectrum and  $[ ]^*$  is complex conjugation. The specification of  $\Delta t = t_2 - t_1$  makes explicit the time delay taken for the time-reversal process between the forward probe signal propagation and the backpropagation from the TRM. As mentioned above, we assumed that environmental changes during the short time interval of the two-way propagation between the PS and TRM are negligible. The calculated time-reversed acoustic fields then were inverse Fourier transformed to obtain the pressure time series at  $\mathbf{r} = (r, z)$ .

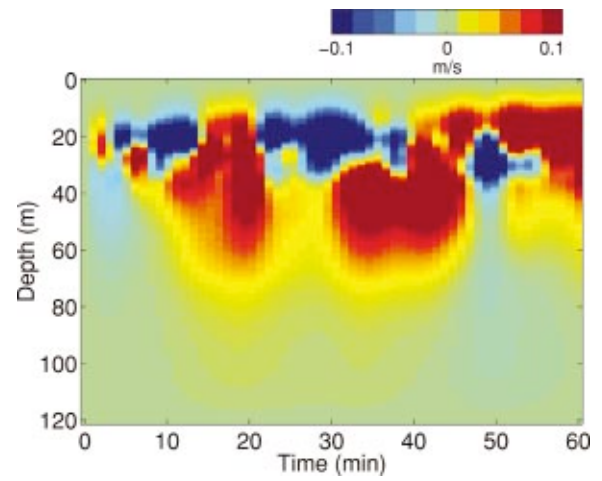


FIG. 10. Simulated sound-speed perturbations averaged in range over 8 km. The positive perturbation means increased sound speed due to the downward displacement of the internal waves.

## B. Simulation results

Here we describe the simulation results based on the methods described above. A special emphasis is given to the relationship between the sound-speed perturbations and the changes of focal structure as well as the intensity variations at the PS position. The results provide physical insight into how the time-evolving ocean environment affects the variation of the spatial focal structure.

Figure 10 shows one hour of the simulated sound-speed perturbations. Although full range-dependent sound-speed data was used for the propagation modeling, to make the complicated three-dimensional (range, depth, and time) data understandable it is represented here as the perturbed sound speed from the sound-speed distribution at  $t = 0$  min and averaged over the 8 km range between the TRM and PS,

$$\delta c(z, t) = \frac{1}{R} \int_0^R [c(r, z, t) - c(r, z, 0)] dr, \quad (5)$$

where  $R$  is the distance between the TRM and PS. Thus, no perturbation exists at zero minute. The positive perturbation indicates an increase in sound speed resulting from the net effect of the downward displacement of internal waves between the TRM and PS. This specific one hour realization shows two big downward internal wave displacements between 10 and 50 min. During this downward motion, the upper part of the water column also shows negative sound-speed perturbations, indicating that more than two internal wave modes are involved in this event.

Figure 11(a) shows the simulated single-frequency (3.5 kHz) focal structures at four different times (0, 10, 40, and 50 min) using the same probe signal received at 0 min. The probe signal was excited at a depth of 60 m and 8 km away from the TRM. The intensity field was normalized by the value at  $t = 0$  min obtained at the probe source position. The focal size at 0 min is about 2 m in depth and 200 m in range at the 3 dB down points, which is similar to the vertical focal size measured during the experiment, as shown in Figs. 5, 6, and 7. At 10 min, the downward internal wave motion starts to perturb the sound speed from the upper part of the water

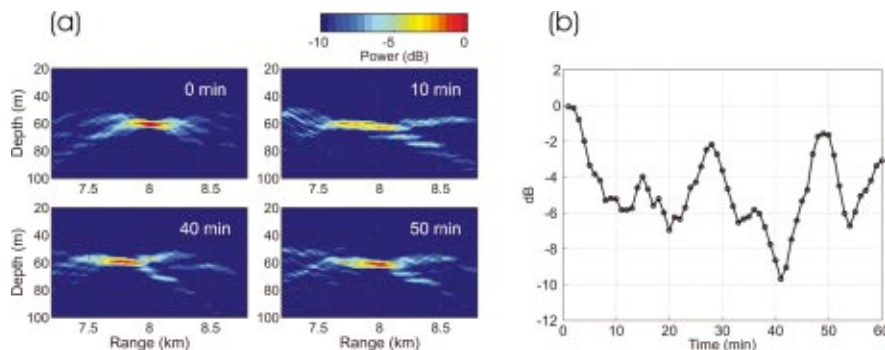


FIG. 11. Simulated single frequency time-reversal foci at 3.5 kHz. (a) Time-reversal foci at four different times (0, 10, 40, and 50 min) using the same probe signal received at 0 min from the range of 8 km and depth of 60 m. (b) The variation of the focal intensity of the time-reversal foci at the position of PS.

column (Fig. 8). Although the unperturbed lower-order modes that are trapped under the thermocline still establish a focus at the original position of the PS, the perturbed higher-order modes tend to move the focus toward the TRM, resulting in the extended focal size in range and the degradation of the focal intensity. At 40 min, a large internal wave motion causes a positive sound-speed perturbation in the upper-half part of the water column. Now all the propagating modes are perturbed in the same direction and make a focal shift toward the TRM by 200 m without much degradation of the intensity at the shifted focal center. At the PS range (8 km), the sidelobes at the end of the focus dominate the structure, which is divided into two parts as observed in the experiment. This suggests that in the experiment we were looking at the outside of the focus during the divided focal structure and the focal center was shifted in range without disappearing. As the sound-speed perturbation decreases the focus returns to the original position at 50 min. As observed in the simulation results, the changes in the vertical focal size is negligible during the one hour period while the size and position of the horizontal focal structure is quite variable.

The variation of the focal strength at the probe source position is depicted in Fig. 11(b). The intensity level is normalized by the strength at 0 min. Therefore, the negative values mean intensity degradation due to the sound-speed mismatch. The intensity curve starts at 0 dB as a maximum and runs up and down according to the degree of sound-speed perturbation. As discussed, the degradation for the first 10 min is due to the extended and diffused focal structure resulting from the sound-speed changes in the upper part of the water column. The minimum intensity level appears as a 10 dB degradation around 40 min resulting from the focal shift. The focal strength recovers up to  $-2$  dB at 50 min when the mismatch is minimized.

The simulation results seem to have captured the characteristics of the measured data shown in Figs. 6 and 7. The main features are splitting of the focal structure associated with the large intensity drop at the corresponding time and remerging of the focus later at the correct position. The simulation results also show that the focal strength is closely related to the focal shift due to the sound-speed mismatch between the forward probe signal propagation and the backpropagation of the time-reversed signal. The intensity variation should be higher in the higher-frequency transmission for the same distance of focal shift, as described in the next section.

## V. THEORETICAL ANALYSIS OF FOCAL SHIFT AND DEGRADATION

This *environmentally driven* focal shift is similar to the offset of the estimated source location in matched-field processing called a mirage.<sup>22</sup> In Ref. 22, the offset or error in the source localization was due to the mismatch between the model bathymetry used for the calculation of the replica fields and the real bathymetry of the experimental area. A slight frequency change between the forward and backward propagation in time reversal also provides a shift in focal range.<sup>7,23</sup> This technique is based on waveguide-invariant theory,<sup>10,11,13</sup> which explains the linear relationship between the rate of the change of the phase along the waveguide and the rate of change of the acoustic frequency. Here, we examine the focal shift associated with the frequency change as well as the environmental variation together using a generalized waveguide-invariant theory.<sup>12</sup> This investigation provides a clue for developing a method of robust focusing, which is discussed in the next section.

We employ the adiabatic normal mode theory<sup>24</sup> to describe acoustic propagation in a range-dependent ocean, assuming that the ocean environment changes gradually in range. Although mode coupling effects are not negligible for 3.5 kHz transmissions, the approach still is useful to explain the main features in the case of small environmental fluctuations and sufficient to provide physical insight into how focal shift and intensity degradation are related with various waveguide and acoustic parameters. The sound-pressure field received at a range  $r=0$  and depth  $z$  due to a point source of unit strength at  $r=R$  and  $z=z_s$  can be written as

$$p(0,z) = \frac{\sqrt{2\pi i}}{\rho(z_s)} \sum_n \frac{u_n(R,z_s)u_n(0,z)}{\sqrt{\bar{\xi}_n R}} \exp(i\bar{\xi}_n R), \quad (6)$$

where  $i = \sqrt{-1}$ ,  $u_n$  is the local modal function, and  $\bar{\xi}_n$  is the range-averaged horizontal wave number given by  $\bar{\xi}_n = R^{-1} \int_0^R \xi_n dr$ . Normally, horizontal wave numbers are complex and can be divided into the real and imaginary part as  $\bar{\xi}_n = \bar{k}_n + i\bar{\alpha}_n$ .

Substituting Eq. (6) into Eq. (4), ignoring the small changes of the modal functions during the elapsed time  $\Delta t = t_2 - t_1$  for the time-reversal process, and using the orthogonality property of mode functions, the time-reversed acoustic field at a field point can be written as

$$p_N(r, z, \Delta t) \sim \sum_n A_n \exp[-\bar{\alpha}_n(R+r)] \times \exp i[\bar{k}_n(t_2)r - \bar{k}_n(t_1)R], \quad (7)$$

where

$$A_n \approx \frac{u_n(r, z)u_n(R, z_s)}{\rho(z_s)\sqrt{\xi_n^2 r R}}. \quad (8)$$

Here we keep the variation of horizontal wave numbers in the phase term but the variations are ignored in the modal attenuation and amplitude term  $A_n$ .

The intensity field around the PS position can be written as

$$I(r, z, \Delta t) \equiv |p_N|^2 \sim \sum_{n,m} A_m A_n \exp[-\bar{\alpha}_{mn}(R+r)] \times \cos[\Delta\bar{k}_{mn}(t_2)r - \Delta\bar{k}_{mn}(t_1)R], \quad (9)$$

where  $\bar{\alpha}_{mn} = \bar{\alpha}_m + \bar{\alpha}_n$  is modal attenuation and  $\Delta\bar{k}_{mn} = \bar{k}_m - \bar{k}_n$  is the real part of the wave number difference between the mode numbers  $m$  and  $n$ . A perturbed horizontal wave number difference  $\delta\Delta\bar{k}_{mn}$  due to small changes in sound speed  $\Delta c(r, z)$ , bathymetry  $\Delta h(r)$ , or acoustic frequency  $\Delta\omega$  during the time  $\Delta t$  can be expressed as

$$\Delta\bar{k}_{mn}(t_2) \approx \Delta\bar{k}_{mn}(t_1) + \delta\Delta\bar{k}_{mn}(\Delta c, \Delta h, \Delta\omega). \quad (10)$$

At range  $r=R$ , the closure property of the modes,  $\sum_n u_n(z)u_n(z_s)/\rho(z_s) \approx \delta(z-z_s)$  and  $\delta(z)$  is the Delta function, implies that the focus is at the depth  $z=z_s$ . However, the modal attenuation and the perturbed modal wave number difference degrade the focal strength by

$$\exp(-2\bar{\alpha}_{mn}R)\cos(\delta\Delta\bar{k}_{mn}R). \quad (11)$$

The modal attenuation degrades the focus by reducing the amplitude of the intensity field while the perturbed modal wave number difference degrades the focus by shifting the focal center to a different range since it is associated with the phase term.

According to first-order perturbation theory, the perturbed modal wave number caused by small changes in sound speed  $\Delta c(r, z)$  or frequency  $\Delta\omega$  can be represented as<sup>25</sup>

$$\delta\bar{k}_n = \frac{1}{2\bar{k}_n} \int_0^\infty \frac{\delta\bar{q}|u_n(z)|^2}{\rho(z)} dz, \quad (12)$$

where  $\bar{q} = (\omega/\bar{c})^2$  and  $\delta\bar{q}$  is due to either sound-speed or frequency perturbations. For arbitrary sound-speed profiles, Eq. (12) can be used to calculate the phase term in Eq. (11). Analytic forms of horizontal wave numbers are known for some simple waveguide conditions.<sup>11,24</sup> One of them is the ideal waveguide for which the horizontal wave number is  $k_m = \sqrt{(\omega/c)^2 - (m\pi/h)^2}$ , where  $c$  is the homogeneous sound speed and  $h$  is the water depth. The wave number difference then can be represented as

$$\Delta k_{mn}(c, h, \omega) \approx \frac{\pi^2(n^2 - m^2)}{2} ch^{-2} \omega^{-1}, \quad (13)$$

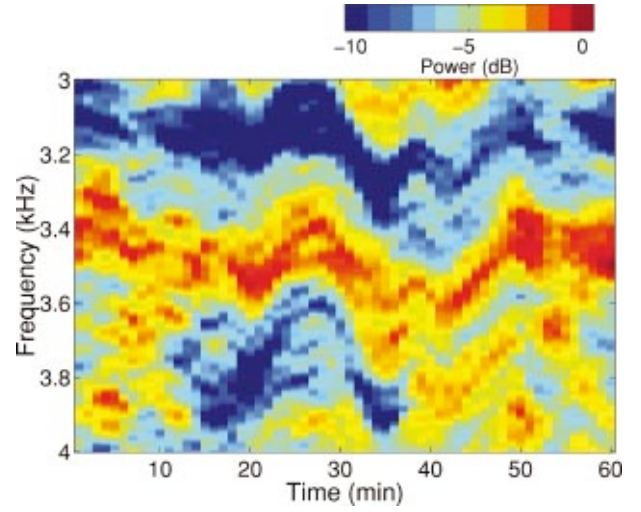


FIG. 12. Spectrogram of the simulated acoustic field of one-way propagation between the PS and a TRM element (77 m). The result shows the shift of frequency of the high-intensity zone with changing sound-speed conditions.

which is true for high-frequency propagation with a large number of modes.<sup>11</sup>

A measure of focal shift caused by perturbation of the wave number difference  $\Delta\bar{k}_{mn}$  is obtained by following the stationary phase (constant intensity lines) in Eq. (9). Defining  $\Phi \equiv \Delta\bar{k}_{mn}r$ , the stationary phase condition becomes

$$\delta\Phi = \frac{\delta\Delta\bar{k}_{mn}}{\Delta\bar{k}_{mn}} + \frac{\delta r}{r} = 0. \quad (14)$$

Inserting Eq. (13) into Eq. (14) and taking derivatives with respect to  $h$  and  $\omega$ , the stationary phase condition leads to the expression of waveguide-invariant theory for an ideal waveguide,<sup>12</sup>

$$\frac{\delta r}{r} = \frac{1}{\beta} \frac{\delta\omega}{\omega} - \frac{\gamma}{\beta} \frac{\delta h}{h}, \quad (15)$$

where  $\beta=1$  and  $\gamma=-2$ . This expression describes the focal shift induced by a change in frequency or water depth in an ideal waveguide. The relationship between the first two terms indicates that increasing the frequency leads to increasing the focal range, which has been used for variable range focusing in the time-reversal process.<sup>7,23</sup> The relationship between the first term and the third term shows that increasing the channel depth also increases the focal range, which was observed as a mirage effect in matched-field processing<sup>22</sup> and a shift of interference patterns caused by tidal variations.<sup>26</sup> This expression also explains the internal-wave-induced focal shift observed in the simulation results. The internal-wave displacement changes the thermocline depth. Changing the thermocline depth has the same effect as changing the effective waveguide depth for the acoustic modes trapped below the thermocline. Equation (15) indicates that the downward internal-wave displacement (reduced channel depth) moves the focal structure toward the TRM (reduced focal range), as observed in the simulation. The distance of focal shift is independent of frequency for the same amount of channel depth (sound-speed) variation

while the acoustic fluctuation normally is greater at higher frequency due to the smaller focal size.

Equation (15) also contains information about the relationship between a change of frequency and a change of channel depth. At the fixed range  $R$ , a change in channel depth results in a change in the frequency content of the intensity field. Figure 12 is a spectrogram of the simulated intensity field generated by the one-way propagation between the PS and a receiver (77 m) of the TRM. The spectrogram shows the positive frequency shift as the internal wave moves downward, as indicated by Eq. (15). This is simply an interference phenomenon and does not imply a nonlinear process. The frequency shift caused by hydrodynamic variability including internal waves has been discussed earlier.<sup>27-30</sup>

In other waveguide conditions, the parameters  $\beta$  and  $\gamma$  in Eq. (15) have different values<sup>12</sup> for a different group of modes. Specifically for  $\beta$ , from the definition of the relationship between the change in horizontal wave number difference and the change in frequency,

$$\frac{\delta\Delta\bar{k}_{mn}}{\Delta\bar{k}_{mn}} \equiv -\frac{1}{\bar{\beta}_{nm}} \frac{\delta\omega}{\omega}, \quad (16)$$

where  $\bar{\beta}_{nm}$  can be simply calculated using the modal slowness,<sup>13</sup>

$$\bar{\beta}_{nm} = -\frac{\Delta\bar{k}_{mn}/\omega}{\delta\Delta\bar{k}_{mn}/\delta\omega} = -\frac{\Delta\bar{s}_{p,mn}}{\Delta\bar{s}_{g,mn}}. \quad (17)$$

Here  $\Delta\bar{s}_{g,mn} = \bar{s}_{g,m} - \bar{s}_{g,n}$  and  $\Delta\bar{s}_{p,mn} = \bar{s}_{p,m} - \bar{s}_{p,n}$ . The  $\bar{s}_{g,m}$  and  $\bar{s}_{p,m}$  are the range-averaged modal group slowness and modal phase slowness of mode  $m$ , respectively. When multiple mode groups are involved, focal shifting inevitably is accompanied by a focal strength degradation. However, the perturbed horizontal wave numbers between the modes within a dominant modal group can have a high correlation resulting in a shift of the focal structure back and forth around the PS, as observed in the simulation results.

## VI. ADAPTIVE TIME REVERSAL

Now that we have some quantitative understanding of the nature of the focal instability, we investigate methods for robust time-reversal focusing. The methods involve modifying the received probe signal to make it more robust to the time-evolving ocean environment. Simulation results based on the suggested methods are discussed.

### A. Adaptive MFP versus TRP

Given Eq. (11), a direct approach for reducing the sensitivity of the time-reversal process to sound-speed variations is minimizing the effect of  $\cos(\delta\Delta\bar{k}_{nm}R)$  by modifying the received signal to a form suitable for the backpropagation environment. Without having exact *a priori* environmental information along the propagation path, one possible method is to reconstruct the received signal in a form that spans the range of possible wave-front perturbations. By backpropagating a signal representing the multiple wave fronts, we can

minimize the phase perturbation and avoid the case of the extreme mismatch between forward propagation and back-propagation.

Considering the similarity between matched-field processing and time-reversal processing,<sup>14</sup> adaptive methods developed for robust MFP<sup>31</sup> can be applied to TRP. A simple approach for robust MFP is to use multiple replica-vector constraints, e.g., multiple location constraints (MLC)<sup>32</sup> or multiple sound-speed constraints (MSC).<sup>33</sup> The MLC method utilizes multiple neighboring points to construct a replica vector. The MSC method makes use of multiple sound-speed profiles obtained from several measurements or an archived database to generate the possible wave-front perturbations in a particular geographical region. These methods easily can be implemented with computer-generated replica fields. To apply these methods to TRP, we need to modify the measured probe signal rather than the replica fields since the ocean itself generates the replica fields in TRP. This requires additional measurements, e.g., multiple probe signals obtained at different locations or under different sound-speed conditions over time, which might not be possible in practice.

As discussed in the previous section, the frequency can be another choice as a parameter for multiple constraints since the waveguide invariant theory relates the frequency shift to the focal range shift, water depth, and sound speed. In addition, time-reversal focusing using multiple frequency constraints (MFC) requires only a single transmission of a broadband pulse as opposed to the MLC and MSC, which involve multiple probe signals.

## B. Methods

The first step of adaptive TRP is constructing a probe signal matrix by gathering multiple probe signal vectors as

$$\mathbf{P}(\omega) = [\mathbf{p}_1, \mathbf{p}_2, \dots, \mathbf{p}_N], \quad (18)$$

where  $\mathbf{P}$  is a  $J \times N$  probe signal matrix at frequency  $\omega$  and each element  $\mathbf{p}_n$  is a  $J \times 1$  signal vector.  $J$  is the number of transducers in the TRM and  $N$  is the number of probe signal vectors received by the TRM. The vectors  $\mathbf{p}_n$  have different meanings in the MLC, MSC, and MFC methods. In the MLC method, the vectors represent narrow band signals received from probe sources at different ranges:

$$\mathbf{p}_n = G(\mathbf{r}_j; \mathbf{r}_n, t_1, \omega), \quad (19)$$

where  $G(\mathbf{r}_j; \mathbf{r}_n, t_1, \omega)$  is the Green's function at frequency  $\omega$  and  $t = t_1$  between the TRM at  $\mathbf{r}_j$  and the probe source at  $\mathbf{r}_n$ . The known source spectrum  $S(\omega)$  is removed from the received signal. In the MSC method, they are narrow band signals obtained over time, indicating that each vector represents a different sound-speed environment,

$$\mathbf{p}_n = G(\mathbf{r}_j; \mathbf{r}_s, t_n, \omega), \quad (20)$$

where  $G(\mathbf{r}_j; \mathbf{r}_s, t_n, \omega)$  is the Green's function obtained at  $t = t_n$  from a probe source located at  $\mathbf{r}_s$ . In the MFC method, each vector corresponds to a different frequency component extracted from a single broadband pulse,

$$\mathbf{p}_n = G(\mathbf{r}_j; \mathbf{r}_s, t_1, \omega_n), \quad (21)$$

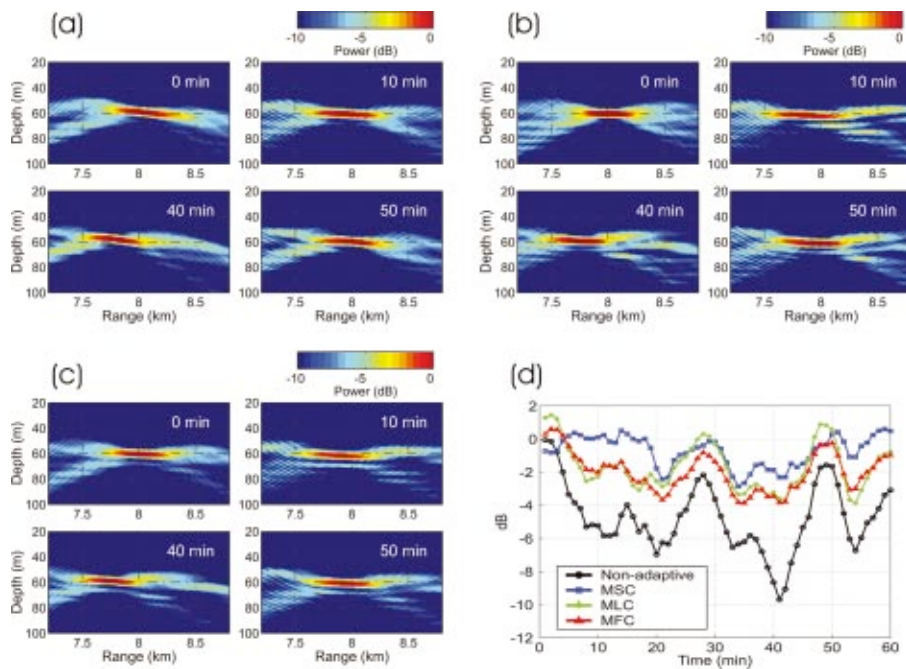


FIG. 13. Simulated single frequency time-reversal foci at 3.5 kHz using adaptive methods: (a) multiple sound-speed constraints (MSC); (b) multiple location constraints (MLC); and (c) multiple frequency constraints (MFC). Also shown in (d) is a comparison of the variation of the time-reversal focal strength at the probe source position (range at 8 km and depth at 60 m).

where  $\omega_n$  is a frequency bin around  $\omega$ . The performance of the adaptive methods depends on the similarity between the signal matrix constructed from the multiple constraint methods and the possible signal forms in the backpropagation environment. The signal vectors thus should be measured with enough time covering the possible oscillations of the internal waves in MSC, with ranges of the possible focal shifts in MLC around the probe source but not exceeding the focal size,<sup>32</sup> and with the corresponding frequency range in MFC (typically within 10% of the center frequency).

The next step is to derive a *field vector* that will be used for backpropagation. Here, we simply follow the procedure described in Ref. 33. If we take many probe signal pings or frequency bins, the number of probe signal vectors spanning all possible wave-front perturbations can be large. However, this does not mean the effective dimension of the perturbation space also is large. The modal phase perturbation can be highly correlated among the modes as well as signal pings. The dimension actually is determined by the number of effective internal wave modes interacting with acoustic modes. Normally, internal waves can be represented by a few modes in shallow water.<sup>20</sup> The design of an efficient constraint space for the signal vector consists of selecting the minimum number of vectors that can best approximate the phase perturbation space. This dimension reduction can be achieved using the singular value decomposition (SVD) of the signal matrix  $\mathbf{P}$  with a rank  $K$  approximation,

$$\mathbf{P}(\omega) = \mathbf{U}\mathbf{\Sigma}\mathbf{V}^+, \quad (22)$$

where  $[\ ]^+$  is the Hermitian transpose,  $\mathbf{U}$  is a  $J \times K$  matrix whose columns are the left singular vectors,  $\mathbf{\Sigma}$  is a  $K \times K$  matrix whose diagonal elements are the singular values of  $\mathbf{P}$ , and  $\mathbf{V}$  is a  $N \times K$  matrix whose columns are the right singular vectors. Here  $J$  is the number of receivers in the TRM, and  $N$  is the number of probe-source pings or frequency bins observed. Now the field vector  $\mathbf{H}$  for backpropagation can be

obtained from a linear combination of the left singular vectors,

$$\mathbf{H}(\omega) = \mathbf{U}(\omega)\mathbf{q}, \quad (23)$$

where  $\mathbf{q}$  is a  $K \times 1$  vector representing the contributions of each singular vector. The singular values tend to decrease rapidly with an increasing number such that the first singular vector corresponding to the largest singular value can be sufficient as a field vector for stable focusing, i.e.,  $\mathbf{q} = [1, 0, \dots, 0]^T$ . In other words, the effective rank of the matrix  $\mathbf{P}$  is equal to one.

The final step is to replace  $G(\mathbf{r}_j; \mathbf{r}_s, t_1, \omega)$  in Eq. (4) with  $\mathbf{H}(\omega)$  in Eq. (23). Then the adaptive time-reversed pressure field becomes

$$p_A(\mathbf{r}, t_2, \omega) = \sum_j S^*(\omega) H^*(\mathbf{r}_j, \omega) G(\mathbf{r}; \mathbf{r}_j, t_2, \omega). \quad (24)$$

This approach should provide a stable focal structure since the field vector  $H(\mathbf{r}_j, \omega)$  was chosen to maintain a high correlation with  $G(\mathbf{r}; \mathbf{r}_j, t_2, \omega)$  for all possible wave front perturbations. The above SVD process smears out the perturbation of the high-order modes that are most affected by the internal waves in a downward refracting environment. The backpropagated fields then are missing these perturbed higher-order modes resulting in the increased focal size. This has the same effect as selectively increasing the waveguide attenuation.

### C. Numerical examples

We start with an example of single-frequency (3.5 kHz) time-reversal foci simulated using the proposed adaptive methods (MSC, MLC, and MFC). The field vector for each method was derived from the signal matrix  $\mathbf{P}(\omega)$  constructed as follows. For the MSC method, 24 signal vectors (5 min intervals) were calculated using two hours of sound-speed data before starting backpropagation. For the MLC method,

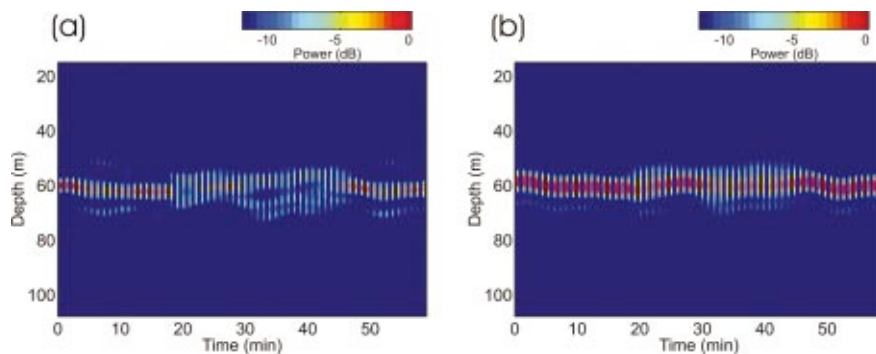


FIG. 14. Simulated 10 ms time-reversed pulse at the probe source range (8 km) (a) with the nonadaptive method and (b) with the adaptive method.

15 signal vectors were calculated using the probe sources distributed every 20 m in range spanning 7.85–8.15 km. Last, for the MFC method, 30 frequency bins spanning 3.2–3.8 kHz were extracted from a single broadband pulse calculated with the sound-speed environment at 0 min. The derived field vectors were used to evaluate backpropagation focusing at the center frequency for the next one hour period, which was the same time period used for simulation of the nonadaptive method in Fig. 11. To compare these results with those of the nonadaptive method, the intensity field was normalized using the intensity field of the nonadaptive method as

$$I(r, z, t) = 10 \log \left( \frac{|p_A(r, z, t)|^2}{|p_N(r_s, z_s, 0)|^2} \right), \quad (25)$$

where  $I$  is the normalized intensity field,  $p_A$  is the time-reversed pressure field with the adaptive methods, and  $p_N(r_s, z_s, 0)$  is the time-reversed pressure field with the nonadaptive method at  $t=0$  min obtained at the probe source position.

The results (Fig. 13) clearly show that the focal size becomes larger with adaptive methods. The horizontal focal size is about 400 m and the vertical focal size is about 4–5 m at the 3 dB down points, which is twice as large as the focal size of the nonadaptive method. The focal intensity remains strong at 10 min while it showed a diffused pattern with the nonadaptive method. Although focal shifts are also observed with the adaptive methods, the increased focal size helps avoid extreme intensity drops caused by the focal shift, as seen at 40 min in the nonadaptive result. As shown in Fig. 13(d), the adaptive methods consistently show higher-intensity levels than those of the nonadaptive method. In this specific case, MSC shows better performance and the results from the other two methods (MLC and MFC) are similar to each other. As mentioned previously, the performance depends on the similarity between the field vector derived from the signal matrix and the signal forms in the backpropagation environment. In this case, the two hour period for MSC appears to be long enough to better cover the possible wavefront perturbation than the range and frequency spans used for the other two methods. At times the intensity level goes above 0 dB resulting from the increased total power in adaptive methods. In this simulation, the power of the adaptive field vectors were larger by 65% (MSC), 48% (MLC), and 40% (MFC) than that of the nonadaptive method, resulting in approximately 2 dB higher intensity. Here we used about

$\pm 2\%$  range span ( $\delta r/r$ ) for MLC for the calculation of the field vectors but had to use about  $\pm 8.6\%$  frequency span ( $\delta \omega/\omega$ ) for MFC to obtain a similar result. This indicates that the parameter  $\beta$  of the dominant mode group is larger than 1 in this sound-speed environment.

Last, Fig. 14 shows the simulation of a 10 ms pulse backpropagated every minute for one hour from a TRM and received by a vertical-receiver array located at the PS range. In the nonadaptive method, the received probe pulse was time reversed and transmitted without modification. In the adaptive method (MFC), the field vector was obtained using a probe signal covering the same frequency band ( $\pm 300$  Hz). Since the pulse is relatively narrow band, we used the single field vector  $\mathbf{H}$  obtained at the center frequency 3.5 kHz for all of the frequency bins of the 10 ms pulse. As expected, the vertical focal sizes are larger with the adaptive method. The nonadaptive method also shows a split focal structure between 20 to 45 min. The adaptive method removes this feature and maintains a single focal structure throughout the entire 60 min period.

## VII. SUMMARY

We have investigated the stability of time-reversal focal structures with both experimental data and numerical simulations. As expected, the high-frequency TRM (3.5 kHz) was sensitive to the fluctuating ocean environment such that a stable focus was limited to on the order of few tens of minutes, which is in contrast to several hours to days at 450 Hz. Numerical simulations involving sound speed fluctuations due to internal waves demonstrated that the focal intensity does not decrease linearly with time but shows focal splitting and recombination associated with a focal shift caused by phase changes in the acoustic field. Using waveguide-invariant theory, the focal range shift was related to the frequency shift and channel depth changes.

A qualitative and quantitative understanding of the nature of focal stability provided guidance for developing robust time reversal focusing methods in fluctuating ocean environments. The basic idea is to find an adaptive weight vector representing all possible perturbations using the SVD prior to backpropagation. Among the three different multiple constraint methods (MLC, MSC, and MFC) considered, numerical simulations showed that the MFC is the most efficient method to extend the period of stable focusing since it requires just a single transmission of a broadband probe signal.

## ACKNOWLEDGMENTS

This research was supported by the Office of Naval Research, Grant No. N00014-01-D-0043-D06.

## APPENDIX: INTERNAL WAVE SIMULATION

Here we briefly describe the internal wave model following the approach developed by Henyey *et al.*<sup>17</sup> with a little modification in the internal-wave energy spectrum. The vertical displacement  $\eta(r, z, t)$  of an internal wave can be expressed as a sum of discrete normal modes as

$$\eta(r, z, t) = \int_0^{2\pi} \int_{\omega_l}^{N_{\max}} \sum_l f(\omega, l, \theta) \phi_l(\omega, z) \times \exp i(k_h r \cos \theta - \omega t) d\omega d\theta, \quad (\text{A1})$$

where  $\omega_l$  is the local inertial frequency,  $N_{\max}$  is the maximum buoyancy frequency, and  $k_h$  and  $\phi_l$  are the horizontal wavenumber of the  $l$ th mode and the vertical mode function, respectively. The displacement field  $\eta(r, z)$  at a given time is a two-dimension cut of a three-dimensional internal wave field propagating from all azimuthal directions. The dispersion relation  $\omega(k_h)$  and eigenfunctions  $\phi_l(\omega, z)$  are determined by the second-order differential equation,

$$\frac{d^2 \phi_l}{dz^2} + k_h^2 \left[ \frac{N^2(z) - \omega^2}{\omega^2 - \omega_l^2} \right] \phi_l = 0, \quad (\text{A2})$$

subject to the boundary conditions  $\phi_l(0) = \phi_l(D) = 0$ , where  $D$  is water depth,  $N(z)$  is the buoyancy frequency.  $F(\omega, l) = \int_0^{2\pi} f(\omega, l, \theta) d\theta$  is a zero mean, complex Gaussian random variable associated with the internal-wave power spectrum,<sup>18</sup>

$$|F(\omega, l)|^2 = bE_{\text{GM}} \rho \left( \int N(z) dz \right)^2 H(l) B(\omega), \quad (\text{A3})$$

where  $bE_{\text{GM}}$  is the internal-wave energy parameter,  $\rho$  is the water density and  $H(l)$  is the mode amplitude spectrum given by

$$H(l) = M(l^2 + l_*^2)^{-p/2}, \quad (\text{A4})$$

and  $M$  is a normalization factor such that  $\sum_{l=1}^{l_{\max}} H(l) = 1$ . The  $p$  and  $l_*$  determine the relative mode amplitude by power law. We used the following functional form for the frequency spectrum  $B(\omega)$  which represents the measured spectrum well as shown in Fig. 8(c):

$$B(\omega) = W \frac{\omega_l \sqrt{\omega^2 - \omega_l^2} \sqrt{N_{1/3}^2 - \omega_l^2 + \omega^2}}{\omega^3}, \quad (\text{A5})$$

where  $W$  also is a normalization factor such that  $\int_{\omega_l}^{N_{\max}} B(\omega) d\omega = 1$ . The spectrum decreases with a slope of  $\omega^{-2}$  and then  $\omega^{-2/3}$  from  $N_{1/3} = \int N(z) dz / 3D$ .

The parameters used for the internal wave calculations are  $bE_{\text{GM}} = 0.142$  m,  $p = 4$ ,  $l_* = 1$ , and  $l_{\max} = 15$ . The shortest and longest internal wave wavelengths used for the calculations are 20 m and 50 km. The 50 frequency components were calculated on a linear scale between the corresponding wave numbers, 0.000 126 and 0.3142 rad/m. We assumed

that the internal wave field is horizontally isotropic. Each directional component was calculated for 2° intervals and integrated over all directions.

- <sup>1</sup>A. Parvulescu and C. S. Clay, "Reproducibility of signal transmissions in the ocean," *Radio Electron. Eng.* **29**, 223–228 (1965).
- <sup>2</sup>M. Fink, C. Prada, F. Wu, and D. Cassereau, "Self focusing with time reversal mirror in inhomogeneous media," *Proceedings of the IEEE Ultrasonics Symposium*, 1989, Montreal, 1989, pp. 681–686.
- <sup>3</sup>D. R. Jackson and D. R. Dowling, "Phase conjugation in underwater acoustics," *J. Acoust. Soc. Am.* **89**, 171–181 (1991).
- <sup>4</sup>W. A. Kuperman, W. S. Hodgkiss, H. C. Song, T. Akal, C. Ferla, and D. Jackson, "Phase conjugation in the ocean: Experimental demonstration of an acoustic time-reversal mirror," *J. Acoust. Soc. Am.* **102**, 25–40 (1998).
- <sup>5</sup>D. R. Dowling and D. R. Jackson, "Narrow-band performance of phase-conjugate arrays in dynamic random media," *J. Acoust. Soc. Am.* **91**, 3257–3277 (1992).
- <sup>6</sup>M. Dungan and D. R. Dowling, "Computed narrow-band time-reversing array retrofocusing in a dynamic shallow ocean," *J. Acoust. Soc. Am.* **107**, 3101–3112 (2000).
- <sup>7</sup>W. S. Hodgkiss, H. C. Song, W. A. Kuperman, T. Akal, C. Ferla, and D. R. Jackson, "A long range and variable focus phase conjugation experiment in shallow water," *J. Acoust. Soc. Am.* **105**, 1597–1604 (1999).
- <sup>8</sup>G. F. Edelmann, T. Akal, W. S. Hodgkiss, S. Kim, W. A. Kuperman, and H. C. Song, "An initial demonstration of underwater acoustic communication using time reversal," *IEEE J. Ocean. Eng.* **27**, 602–609 (2002).
- <sup>9</sup>H. C. Song, W. A. Kuperman, W. S. Hodgkiss, T. Akal, and P. Guerrini, "Demonstration of a high frequency acoustic barrier with a time reversal mirror," *IEEE J. Ocean. Eng.* (in press).
- <sup>10</sup>S. D. Chuprov, "Interference structure of a sound field in a layered ocean," in *Acoustics of the Ocean*, edited by L. M. Brekhovskikh and I. B. Andreevov (Nauka, Moscow, 1982).
- <sup>11</sup>L. M. Brekhovskikh and Y. P. Lysanov, *Fundamentals of Ocean Acoustics* (Springer, Verlag, Berlin, 1991).
- <sup>12</sup>G. A. Grachev, "Theory of acoustic field invariants in layered waveguide," *Acoust. Phys.* **39**, 33–35 (1993).
- <sup>13</sup>G. L. D'Spain and W. A. Kuperman, "Application of waveguide invariants to analysis of spectrograms from shallow water environments that vary in range and azimuth," *J. Acoust. Soc. Am.* **106**, 2454–2468 (1999).
- <sup>14</sup>W. A. Kuperman and D. R. Jackson, "Ocean acoustics, matched-field processing and phase conjugation," in *Imaging of Complex Media With Acoustic and Seismic Waves in Topics of Applied Physics*, edited by X. Fink *et al.* (Springer-Verlag, Berlin, 2002), Vol. 84, pp. 43–97.
- <sup>15</sup>S. Kim, G. F. Edelmann, W. A. Kuperman, W. S. Hodgkiss, H. C. Song, and T. Akal, "Spatial resolution of time-reversal arrays in shallow water," *J. Acoust. Soc. Am.* **110**, 820–829 (2001).
- <sup>16</sup>W. S. Hodgkiss, J. D. Skinner, G. E. Edmonds, R. A. Harriss, and D. E. Ensberg, "A high frequency phase conjugation array," in *Proceedings of Oceans 2001*, 2001, pp. 1581–1585.
- <sup>17</sup>F. S. Henyey, D. Rouseff, J. M. Grochocinski, S. A. Reynolds, K. L. Williams, and T. E. Ewart, "Effects of internal waves and turbulence on a horizontal aperture sonar," *IEEE J. Ocean. Eng.* **22**, 270–280 (1997).
- <sup>18</sup>S. Flatte, R. Dashen, W. Munk, K. Watson, and F. Zachariasen, *Sound Transmission Through a Fluctuating Ocean* (Cambridge University Press, Cambridge, 1979).
- <sup>19</sup>J. A. Colosi and M. G. Brown, "Efficient numerical simulation of stochastic internal-wave-induced sound-speed perturbation fields," *J. Acoust. Soc. Am.* **103**, 2232–2235 (1998).
- <sup>20</sup>T. C. Yang and K. Yoo, "Internal wave spectrum in shallow water: Measurement and comparison with the Garrett–Munk model," *IEEE J. Ocean. Eng.* **24**, 333–345 (1999).
- <sup>21</sup>M. D. Collins, "Generalization of the split-step pade solution," *J. Acoust. Soc. Am.* **96**, 382–385 (1994).
- <sup>22</sup>G. L. D'Spain, J. J. Murray, W. S. Hodgkiss, N. O. Booth, and P. W. Schey, "Mirages in shallow water matched field processing," *J. Acoust. Soc. Am.* **105**, 3245–3265 (1999).
- <sup>23</sup>H. C. Song, W. A. Kuperman, and W. S. Hodgkiss, "A time-reversal mirror with variable range focusing," *J. Acoust. Soc. Am.* **103**, 3234–3240 (1998).
- <sup>24</sup>F. B. Jensen, W. A. Kuperman, M. B. Porter, and H. Schmidt, *Computational Ocean Acoustics* (American Institute of Physics, Woodbury, NY, 1994).
- <sup>25</sup>C. T. Tindle, L. M. O'Driscoll, and C. J. Higham, "Coupled mode pertur-

- bation theory of range dependence,” J. Acoust. Soc. Am. **108**, 76–83 (2000).
- <sup>26</sup> D. E. Weston and K. J. Stevens, “Interference of wide-band sound in shallow water,” J. Sound Vib. **21**, 57–64 (1972).
- <sup>27</sup> V. M. Kuz’kin, “The effect of variability of ocean stratification on a sound field interference structure,” Acoust. Phys. **41**, 300–301 (1995).
- <sup>28</sup> V. M. Kuz’kin, A. V. Ogurtsov, and V. G. Petnikov, “The effect of hydrodynamic variability on frequency shifts of the interference pattern of a sound field in a shallow water sea,” Acoust. Phys. **44**, 77–82 (1998).
- <sup>29</sup> V. M. Kuz’kin, “Frequency shifts on the sound field interference pattern in a shallow water,” Acoust. Phys. **45**, 224–229 (1998).
- <sup>30</sup> V. G. Petnikov and V. M. Kuz’kin, *Shallow Water Variability and Its Manifestation in Interference Pattern of Sound Field*, edited by W. A. Kuperman and G. L. D’Spain (American Institute of Physics, Melville, NY, 2000).
- <sup>31</sup> A. B. Baggeroer, W. A. Kuperman, and P. N. Mikhalevsky, “An overview of matched field methods in ocean acoustics,” IEEE J. Ocean. Eng. **18**, 401–424 (1993).
- <sup>32</sup> H. Schmidt, A. B. Baggeroer, W. A. Kuperman, and E. K. Scheer, “Environmentally tolerant beamforming for high-resolution matched field processing: Deterministic mismatch,” J. Acoust. Soc. Am. **88**, 1851–1862 (1990).
- <sup>33</sup> J. L. Krolik, “Matched-field minimum variance beamforming in a random ocean channel,” J. Acoust. Soc. Am. **92**, 1408–1419 (1992).